Efficient droplet activation of ambient black carbon particles in sub-urban environment

Ping Tian[1], Dantong Liu[2*], Kang Hu[2,3], Yangzhou Wu[2,4], Mengyu Huang[1,5], Hui He[1,5], Jiujiang Sheng[1,5], Chenjie Yu[6], Dawei Hu[7], Deping Ding[1,5]

[1.] Beijing Key Laboratory of Cloud, Precipitation and Atmospheric Water Resources, Beijing Meteorological Service, Beijing, 100089, China

[2.] Department of Atmospheric Sciences, School of Earth Sciences, Zhejiang University, Hangzhou 310058, China

[3] Jiangsu Collaborative Innovation Center of Atmospheric Environment and Equipment Technology, Jiangsu Key Laboratory of Atmospheric Environment Monitoring and Pollution Control, Nanjing University of Information Science & Technology, Nanjing, 210044, China

[4] College of Environmental Science and Engineering, Guilin University of Technology, Guilin, 541006, China

[5] Field Experiment Base of Cloud and Precipitation Research in North China, China Meteorological Administration, Beijing, 100089, China

[6] Université Paris Cité and Univ Paris Est Créteil, CNRS, LISA, Paris, F-75013, France

[7] Department of Earth and Environment Sciences, University of Manchester, Manchester, UK.

Corresponding to: Dantong Liu (dantongliu@zju.edu.cn)

Abstract

The cloud condensation nuclei (CCN) activity of black carbon particles (BC) importantly determines their impacts on cloud microphysics and atmospheric lifetime. This process is crucially influenced by the amount of hygroscopic coating materials that BC acquire during the aging process. It remains a challenge for ambient measurements to capture this process and link this with CCN activity of BC. Here, we directly measured the droplet activation diameter (D50) and activation fraction of BCc ($F_{act,BC}$) in suburban Beijing using coupled measurements of size-resolved number concentrations of CCN at configured water supersaturation (SS) and BC-containing particles (BCc). The number concentration of BCc was found to peak at diameter 180-210 nm after acquiring coatings, larger than that for all particles (50-150 nm). Consequently, the initially smaller BC become enlarged and more hygroscopic, thereby exhibiting CCN activities than other particles. The $F_{act,BC}$ increased from 42% to 69% in number and from 67% to 85% in mass as SS increased from 0.1% to 0.2%, but tended to reach a plateau when SS>0.2%. Notably, $F_{act,BC}$ and D50 linearly correlated with equivalent photochemical age, at a rate of +2% per hour and -3nm per hour, respectively. The results suggest BCc from anthropogenic sources can readily serve as CCN at a relatively low SS, and more than half of the BC population can be activated within a few hours, indicating that the surface-sourced BC can efficiently incorporate into clouds and potentially exert important indirect radiative impacts.

Keywords: black carbon; cloud condensation nuclei; droplet activation fraction; photochemical age

Introduction

Black carbon (BC), a significant anthropogenic pollutant, is generated from the incomplete combustion of fossil fuels and profoundly influences the climate through direct (Ramanathan and Carmichael, 2008; Bond et al., 2013), indirect (Koch et al., 2011), and semi-direct effects (Koch and Del Genio, 2010). The climate response to BC, sensitive to its atmospheric lifetime (Hansen et al., 1997), introduces considerable uncertainty in model studies, attributed to spatial and temporal variations (Park et al., 2005; Koch et al., 2009; Lund et al., 2017).

Wet scavenging, identified as the primary removal mechanism for atmospheric BC (Jacobson, 2010), involves BC particles acting as cloud condensation nucleation (CCN) that are activated into the cloud droplets and removed through precipitation. Although freshly emitted BC particles are generally hydrophobic, they become more hygroscopic through atmospheric processing, acquiring coating materials such as sulfates, nitrates, and secondary organic aerosol compounds, or by coagulating with other particles (Dusek et al., 2006; Tritscher et al., 2011). The increased hygroscopicity of BC enhances their CCN activation efficiency (Weingartner et al., 1995). However, significant variability exists in the literature regarding the extent to which BC acts as CCN (Wu et al., 2019; Rose et al., 2011), due to the diverse properties of BC arising from its various sources and the atmospheric aging process (Henning et al., 2012; Dalirian et al., 2018).

The κ-Köhler theory (Petters and Kreidenweis, 2007), combined with the ZSR mixing rule (Pruppacher and Klett, 1997; Henning et al., 2010), has been successful in predicting the hygroscopicity of internally mixed BC, assuming a spherical core-shell structure. Chamber studies, where the physical and chemical conditions and the initially emitted particles are well controlled, indicate that the hygroscopicity of BC is determined by the fraction and hygroscopicity of the coating material (Snider et al., 2010; Friebel et al., 2019). A relatively thin soluble coating, like 2nm corresponding to about 5% of the total volume for 250nm particles, is enough to make hydrophobic BC CCN active under typical atmospheric supersaturation (Dalirian et al., 2018). The hygroscopic properties of the coating materials can vary significantly; notably, the increase in the hygroscopicity of BC induced by inorganic aerosols (e.g., ammonium nitrate) is more pronounced than that caused by organic aerosols (Kuwata et al., 2007; Liu et al., 2013). However, laboratory experiments often fail to replicate the complexity of

atmospheric conditions; thus, comprehensive field measurements are needed to capture the real-time evolution of the CCN properties of BC.

Despite advancements in understanding the physicochemical transformations of BC through field observations (Liu et al., 2017), quantifying its CCN activity under ambient conditions remains challenging due to the variability in its sources, composition, mixing state, and atmospheric processes (Zhang et al., 2008). Direct field observations indicate that a number fraction of 50%–90% BC can be activated into cloud or fog, depending on the actual ambient supersaturation (Motos et al., 2019a; Motos et al., 2019b;). More than 50% of BC mass can be removed through the wet removal process during transport from the surface to the planetary boundary layer (PBL), as evidenced by studies in East Asian polluted areas (Kondo et al., 2016; Liu et al., 2020). However, determining true ambient supersaturation in in-situ cloud observations is challenging.

The hygroscopicity of BC particles can be derived from their measured mixed state by size-resolved soot particle aerosol mass spectrometer (SP-AMS) (Onasch et al., 2012; Wu et al., 2019), and the hygroscopic tandem differential mobility analyser (HTDMA) under subsaturation condition. However, only a limited number of atmospheric CCN efficiency studies on BC particles have been conducted under water supersaturation conditions. Continuous-flow cloud condensation nuclei counter (CCNc) can measure the CCN number concentration of bulk aerosol under well-controlled supersaturation conditions (Roberts and Nenes, 2005), but it cannot distinguish how much of the BC contributes to activation, given that BC accounts for about 10% of the ambient aerosol. Recently, Hu et al. (2021a) developed a novel method to directly observe the number activation ratios of BC under certain supersaturation levels, based on the size-resolved CCNc and BC measurements, revealing potential overestimation of BC hygroscopicity based on bulk chemical composition.

In this study, continuous observations of the CCN activation and hygroscopic properties of BC under water supersaturation (0.1%, 0.2%, and 0.3%) were conducted during springtime at a suburban site in Beijing. The variation in the hygroscopicity of BC during different pollution levels was investigated through the classification of four distinct air masses types. The equivalent photochemical age (t_{age}), calculated using trace-gas measurements by the Proton-Transfer-Reactor Time-of-Flight Mass Spectrometer, was used to characterize the evolution of BC's CCN activation properties under ambient atmospheric aging.

2. EXPERIMENTAL AND METHODS

2.1. Measurement site and Instrumental Setup

The field campaign was conducted for 33 days from 29th Apr. to 2nd Jun. 2020 at Beijing Cloud Laboratory and Observational Utilities Deployment Base (CLOUD Base) (Tian et al., 2022), approximately 65 km northeast of central Beijing. The main local emissions, which represent a typical suburban environment, originate from industrial, traffic, and residential. Higher pollution conditions at this site were correlated with regional transport of pollutants from the west and south, while cleaner conditions were attributed to dilution by clean air from the northwest (Hu et al., 2022).

The instrument setup is shown in Figure 1a. The bulk and size-resolved physicochemical and hygroscopic properties of aerosols were simultaneously measured during the field campaign. A cyclone $PM_{2.5}$ cut-off inlet (Model: SCC1.829, BGI Inc., USA) was used to remove the coarse mode particles (larger than 2.5μm), and the air was dried by a Nafion tube before entering the instruments. In addition to particle measurement, volatile organic compounds (VOCs) were measured by a Proton-Transfer-Reactor Time-of-Flight Mass Spectrometer (PTR-TOF-MS 8000, Ionicon Analytik GmbH, Innsbruck, Austria) (Fig. 1a).

2.2 Aerosol Chemical Components Measurements and Hygroscopic Growth Factor Calculation

The mass concentration of non-refractory submicron aerosol species, including organic aerosol (OA), chloride (Cl^-), ammonium (NH_4^+), nitrate (NO_3^-), and sulfate (SO_4^{2-}), was measured by an Aerodyne high-resolution time-of-

flight AMS (HR-ToF-AMS, Aerodyne Research Inc., USA). The principles and operation of the HR-ToF-AMS have been detailed in previous publications (Jayne et al., 2000; Drewnick et al., 2005). The HR-ToF-AMS was calibrated before and after the experiment, and relative ionization efficiencies for NH_4^+ (4.0) and SO_4^{2-} (1.2) were calibrated using pure ammonium nitrate and ammonium sulfate, respectively, while default relative ionization efficiency values were used for OA (1.4), NO_3^- (1.1), and Cl^- (1.3) (Middlebrook et al., 2012).

The measurements of individual refractory BC (rBC)-containing particles (BCc) and BC-free particles (BCf) were conducted using the Single Particle Soot Photometer (SP2, DMT Inc., USA). The SP2 uses an intense 1064nm Nd:YAG laser beam to heat BCc to vaporize, with the mass and diameter (*Dc*) of rBC quantified based on the intensity of the incandescence signal. The incandescence signal was calibrated using Aquadag standard (Acheson Inc., USA) and corrected for ambient BC by a factor of 0.75 before the experiment (Laborde et al., 2012). Particles exhibiting only scattering signal were classified as BCf, with their diameters determined based on the intensity of scattering signal and calibrated by polystyrene latex spheres (PSLs). Due to the distortion of the scattering signal caused by the vaporization of the coating material of BCc, the leading edge only (LEO) fitting method was employed to derive the entire size of BCc (Gao et al., 2007; Liu et al., 2014). As suggested by Moteki et al. (2010), for size smaller than 400nm, the scattering signal measured by SP2 is predominantly influence the volume of particle, with little influence from the morphology of BCc. The scattering at λ=1064nm which is larger than the particle size of a typical BCc, can minimize the geometric influence of scattering due to the complex morphology of BC. This is validated to be within 10% accuracy for the optical size determination of BCc at 1064 nm (Hu et al., 2021). Thus, the measured optical diameter by SP2 is assumed to be equal to the volume equivalent diameter (*Dve*) (Hu et al., 2021b). Consequently, the relative bulk volume of coating to BC ($V_{coating}/V_{BC}$) was calculated as the cubic ratio of diameter of *Dve* and *Dc* (Liu et al., 2017):

$$VR = \frac{V_{coating}}{V_{BC}} = \frac{\sum_i D_{ve}^3}{\sum_i D_c^3} - 1 \qquad (1)$$

where D_{ve} is the volume equivalent diameter of the entire BCc, and D_c is the rBC core diameter for the ith single BCc .

The hygroscopic growth factor (κ), which depends on the chemical properties such as molecular weight, dissociate, and osmotic coefficient,can be used to predict the activation properties of particles as CCN under certain supersaturation (SS) (Petters and Kreidenweis, 2007). The κ for all-particles (κ_{all}) was calculated using the Zdanovskii-Stokes-Robinson (ZRS) mixing rule to account for the volume contribution from different chemical components (Mcdonald, 1953). The expression for κ_{all} is:

$$\kappa_{all} = \sum_i \varepsilon_i \, \kappa_i \qquad (2)$$

where κ_i and ε_i represents the hygroscopic growth factor and volume fraction for each chemical component (i.e. $(NH_4)_2SO_4$, NH_4HSO_4, NH_4NO_3, and BC etc.).

The κ of single BCc (κ_{BC}) is dependent on the volume fraction and κ of the coating material, and calculated as:

$$\kappa_{BCc} = \kappa_{coating} \times (\frac{VR}{1+VR}) \qquad (3)$$

where the $\kappa_{coating}$ was selected to match κ_{all}, which represents the average κ of particles, and the $V_{coating}/V_{BC}$ is volume ratios of coating material over the BC, which reflect the coating thickness of BCc particles. This selection is based on the strong correlation, within a 25% variation, between $\kappa_{coating}$ and that of BC-free particles, as previous studies (Liu et al., 2013; Ohata et al., 2016) have demonstrated. Such a correlation is primarily attributed to the similar organic and inorganic compositions of BC-coating materials and BC-free particles (Cui et al., 2022), largely due to internal mixing of these compounds. The κ_{BC} was tested to successfully predict the CCN activation properties of BCc in the field in-situ cloud observation (Motos et al., 2019a).

2.3 Size-resolved CCN Activity of All-particles and BCc

Atmospheric polydisperse aerosols were classified into monodisperse particles at the outlet of a Differential Mobility Analyser (DMA, Model: 3081, TSI Inc., USA). Particles of different mobility sizes were selected by applying varying voltages to the DMA while maintaining a specific sheath flow rate (Knutson and Whitby, 1975). Instead of using the standard TSI Aerosol Instrument Manager control software, the DMA was controlled by custom-made software. This software enabled the selection of specific diameters and control over residence time at those diameters (Moore et al., 2010; Deng et al., 2011). A total of 29 mobility diameters, ranging from 29 nm to 612 nm at logarithmic intervals, were chosen, with each diameter maintained for 30 seconds. This duration was selected considering the time lag, estimated to be less than 20s, between the instruments following the DMA (Fig. 1a). A complete size scan took approximately 15 minutes. The sheath and sample flow rates of the DMA were calibrated both before and after the experiment, and the mobility size selected by the DMA was validated using PSLs.

The monodisperse number concentrations of all condensation nuclei ($[CN]$), $[CCN]$, and both $[BCc]$ and $[BCf]$ were measured using a Condensation Particles Counter (CPC, Model 3772, TSI Inc., USA) with a flowrate of 0.30 L/min, and a Cloud Condensation Nucleus counter (CCNc, DMT Inc., USA) with a flowrate of 0.50 L/min, and another SP2 with a flowrate of 0.12 L/min, respectively (Fig. 1a). Three SSs at 0.1%, 0.2%, 0.3% were set for the CCNc, and with an interval of 30 minutes, allowing for two size scans at each SS. The sample/sheath flowrates and the SS of the CCNc were calibrated before and after the experiment (Rose et al., 2008). Moreover, the monodisperse $[CCN]$, $[CN]$, and $[BCc]$ were corrected for multiple charge effects, a correction applied from large particles (which only with one negative charge) to smaller particles, based on charging probabilities for different mobility size (Wiedensohler, 1988).

The CCN activity of all-particles was determined using the size resolved activation ratio (F_{act}) ($[CCN]/[CN]$), following the method described by Moore et al. (2010). This size-resolved ratio, $[CCN]/[CN]$, indicates the fraction of CN that can serve as CCN, and it can be directly measured by the CCNc and CPC through size scanning with the DMA. The $[CCN]/[CN]$ ratio increase with the particle size, reach 1 for larger particle (e.g., greater than 300 nm), while it decrease to 0 for smaller sizes (e.g., 30 nm). The specific size at which the $[CCN]/[CN]$ ratio equals 0.5 is identified as the activation diameter (D50). This critical value is typically derived through sigmoid fitting of the size-resolved $[CCN]/[CN]$ (Rose et al., 2008).

The CCN activated number concentration of BCc $[BC_{act}]$ is distinguished from BCf and directly measured in this study, following the method by Hu et al. (2021a).This approach compare the difference between the unactivated particle number concentration ($[CN_{unact}]$) and $[BCc]$ to derived how many BCc are activate into CCN. $[CN_{unact}]$ is calculated by subtracting $[CCN]$ from the total $[CN]$. $[CN_{unact}]$ is zero at larger particle sizes, indicating that all particles, including BCc, are activated. Conversely, when $[CN_{unact}]$ equals the total $[CN]$, it signifies that none of the particles are activated. It is well recognized that the activation of BCc into CCN is more unlikely compared to BCf of the same diameter, due to BCc's lower κ (Dusek et al., 2006; Bond et al., 2013). Only when $[CN_{unact}]$ is smaller than $[BCc]$ doesit means some BCc have been activated into CCN. When $[CN_{unact}]$ is zero, it indicates that all BCc are activated. Thus, the $[BC_{act}]$ and activation ratios ($F_{act,BC}$) of BCc are calculated as:

$$[BC_{act}] = [BCc] - ([CN] - [CCN]) \qquad (4)$$

$$F_{act,BC} = ([BC_{act}]/[BCc]) \qquad (5)$$

184   [BC_{act}] is the difference between the [BCc] and [CN_{unact}], and $F_{a,BC}$ is calculated by [BC_{act}] over the [BCc].

185   When [CN_{unact}] is larger than [BCc], it indicates that none of the BCc could be activated, resulting in both [BC_{act}]

186   and $F_{act,BC}$ being 0.

2.4 Determination of the Photochemical Age

188   The mass spectra of VOCs were measured using the PTR-TOF-AMS, calibrated with the CH3COCH4+ (m/z

189   59.0490) and H3O+ (m/z 21.0226), following the procedures described by Bruns et al. (2016). The equivalent

190   photochemical age (t_{age}), a critical factor for assessing the duration of atmospheric photochemical reaction, is

191   derived from comparing the ratios of two VOCs with different OH radical reaction rates, acknowledging that

192   species more reactive with OH diminish more rapidly as photochemical aging increases (Yuan et al., 2012).

193   Despite uncertainties arising from the mixing of fresh emitted and aged air masses, this method provides valuable

194   insights into atmospheric photochemical processing (Parrish et al., 2007). In this study, toluene and benzene were

195   chosen for their strong correlation and differing reaction rates with OH, and expressed as:

196
$$t_{age} = \frac{1}{[OH](k_{toluene}-k_{benzene})} \times \left[\ln\left(\frac{[toluene]}{[benzene]}\right)_0 - \ln\left(\frac{[toluene]}{[benzene]}\right)\right] \quad (6)$$

197   where [OH] is the ambient average OH concentration (2×10^6 molecule cm^{-3}) obtained from the reanalysis

198   product (available from the European Center for Medium Range Weather Forecasts: Atmospheric Composition

199   Reanalysis 4), consistent with previous observation in Beijing (Liu et al., 2018). $k_{toluene}$ and $k_{benzene}$ is the

200   reaction rate with OH of toluene (5.63×10^{-12} cm^{-3} molecule^{-1} s^{-1}) and benzene (1.22×10^{-12} cm^{-3} molecule^{-1} s^{-1}),

201   respectively. $\left(\frac{[toluene]}{[benzene]}\right)_0$ is the ratio of freshly emitted toluene and benzene, and the value was determined to be

202   2.27 ± 0.27 according to the maximum toluene/benzene ratio during the experiment. $\frac{[toluene]}{[benzene]}$ is the ratio of

203   measured toluene and benzene in the atmosphere. The calculation of t_{age} was performed only during daytime

204   ensure it reflects the photochemical process. The dataset of t_{age} in this study has been successfully tested to

205   determine the photochemical reaction or production rates of secondary OA, with further details on the calculation

206   of [OH] and $\frac{[toluene]}{[benzene]})_0$ available in Wu et al., (2022).

2.5. Backward Trajectory Analysis

208   The potential source contribution to the target site was modelled using the Hybrid Single-Particle Lagrangian

209   Integrated Trajectory Model (HYSPLIT) model. Ensemble calculations were performed with 3-hourly, 1°×1°

210   GDAS horizontal and vertical reanalysis wind fields to retrieve 36-hour backward air mass trajectories to the

211   target site. A clustering analysis of the air mass trajectories was conducted using a systematic clustering method

212   (Draxier &Hess, 1998), and a total of 216 trajectories was calculated. The entire observation periods were

213   classified into 4 clusters (Fig. 1b). Cluster 1 (C1) represented the slowest transport values in southern polluted

214   area, while 2 to 4 (C2-C4) originated from the northern clean areas (Fig. 1b).

3. RESULTS AND DISCUSSION

3.1 Overview of Aerosol Physical and Chemical Properties

217   Figure 2a-2d show the time series of aerosol physical and chemical properties, with the colour labels at the top

218   representing different air masses influence periods. The statistical comparison of aerosol properties between

219   different air masses is shown in Fig. 2e-2i. Consistent with previous studies, aerosol physic-chemical properties

220   are highly dependent on air masses (Tian et al., 2020; Zhao et al., 2020). Higher pollutant concentrations,

221   including PM$_1$, Sulphate, Nitrate, OA, and BC, were observed during C1 period with air from the southern part of

222   North China Plain (NCP) (average PM$_1$ value of 33.2 ± 16.4 μg m^{-3}) (Fig. 2e and Fig. 2f), which contains high

pollutant concentrations due to the intensive emissions (Fig. 1b). When the air comes from northern cleaner part of NCP during C3 and C4 periods (Fig. 1b), lower pollutant concentrations were observed (average PM_1 value of 10.4 ± 5.8 μg m^{-3}) (Fig. 2a and Fig. 2e), suggesting that pollutants were diluted and dispersed during the fast transport process. Thus, C1 was estimated as a polluted condition, while C3 and C4 were classified as clean environments. However, C2 originated from the same direction as C4 but with shorter transportation distances, indicating slower wind speeds and less dilution of emissions. Consequently, the PM_1 mass concentration (15.4 ± 10.6 μg m^{-3}) of C2 was higher than that in clean environment but still half lower than that of C1, and classified as light polluted condition (Fig. 2e).

During the transition from clean to pollution condition, the mass concentrations of all chemical components experienced substantial increases, as shown in Fig. 2a. Notably, the increase in inorganic aerosols (including NH_4HSO_4, $(NH_4)_2SO_4$, and NH_4NO_3) was more pronounced than that of OA (Fig. 2b), leading to lower/higher contribution of OA to all-particles during polluted/clean period (Fig. 2b and Fig. 2e). As κ_{all} is determined based on the volume fraction of OA and inorganic aerosol according to the ZSR internal mixing rule, this result distinct κ_{all} characteristic for different airmasses influence periods (Fig. 2d and Fig. 2h).

3.2 The Hygroscopicity of BCc and All-particles

The κ_{all} (particle averaged hygroscopicity) varied from 0.13 to 0.45, with an average value of 0.29 during the observation period (Fig. 2d). The κ_{all} during the polluted C1 period (average value of 0.38) was 1.5 times larger than that during clean C3/C4 period (average value 0.25) (Fig. 2h), attributed to the increased contribution of inorganic aerosol, known for their high hygroscopicity, under polluted condition.

The κ_{BC} is influenced by both κ_{all} and the coating thickness (reflected by $V_{coating}/V_{BC}$) (Eq. 3). The $V_{coating}/V_{BC}$ of BCc during the polluted C1 period was 4.9 ± 4.2, which were about 3 - 5 times larger than that during the clean C3/C4 period (Fig. 3c and Fig. 3g), implying a thick coating of BCc under polluted conditions. Due to the increase in both $V_{coating}/V_{BC}$ and κ_{all}, κ_{BC} exhibited a similar variation characteristic as κ_{all}, with higher values under polluted conditions (average value of 0.23) and lower values under clean conditions (average value of 0.11) (Fig. 2d and Fig. 2h). Many studies assumed the same components between BC coatings and other substances externally mixed with BC (Liu et al., 2013; Ohata et al., 2016), as consistent with the assumption in this study. However, the coatings on BC may contain a higher OA fraction than other BC-free particles (Wang et al., 2020), which means the current calculation may give a higher estimation of κ_{BCc}.

$V_{coating}/V_{BC}$ exhibits a larger variation, ranging from 1.3 to 20, compared to κ_{all}, indicating a substantial influence of $V_{coating}/V_{BC}$ on κ_{BC} (Fig. 2d). This is evidenced by the maximum value of κ_{BC} correlating with that of $V_{coating}/V_{BC}$ (Fig. 2c and Fig. 2d), and the divergence in the maximum values of κ_{all} and κ_{BC} (Fig. 2d). The coating of BCc is formed through by the photo-chemistry of VOCs precursors during the atmosphere aging process, determined by the VOCs precursors and aging time. Compared to the clean clusters C3 and C4, the air mass movement in C1 was much slower, combined with passing the highest pollution level region, the slowly transported air mass from the polluted southern region was characterized with a longer transport time than other air mass clusters (Fig. 1b). As expected, observations from PTR-ToF-MS showed higher VOCs values and a longer t_{age} during the polluted C1 condition (Fig. S2). Figure 2i shows that the t_{age} during polluted C1 period (13h) was about twice as long as that during clean C3/C4 period (9h), reflecting the more aged air during the polluted period.

Figure 3 shows the diurnal variation of PM_1, BC mass concentration, OA fraction, $V_{coating}/V_{BC}$, κ_{all} and κ_{BC} for the different air masses, respectively. More pronounced diurnal patterns were found during the clean C3/C4 period, as the fast-moving clean air masses diluted the pollutant and were mainly influenced by local emissions. However, regional transport and secondary aerosol formation influenced the diurnal pattern during the C1 and C2 periods (Fig. 2a). For chemical inert BC particles, clear BC mass peaks at morning and afternoon rush-hours

267 (marked as grey bar) (Fig. 3b) were observed which is typical time period of heavy traffic with nascent BC
268 emitted, but C1 period showed continuous transport and increased BC mass loading throughout midday, even
269 when the developed planetary boundary layer (PBL) diluted the pollutants.

270 Fresher BCc showed lowest $V_{coating}/V_{BC}$ during morning rush-hours, and within a few hours the $V_{coating}/V_{BC}$
271 quickly increase and peak at noon when solar radiation was strongest for all-time period (Fig. 3d). The increase
272 during midday was in consistent with the OA fraction (Fig. 3c), suggesting that the acquired coating of BC
273 particles might be secondary OA through the photochemical oxidation, in line with recently studies (Cui et al.,
274 2022; Wu et al., 2019). As enhanced OA fraction at noon due to photochemical SOA formation (Fig. 3c), result a
275 lower value of κ_{all} during noontime (Fig. 3e). κ_{BC} is more influenced by $V_{coating}/V_{BC}$, the κ_{BC} was observed
276 increase after morning rush-hours due to the increased of coating on BC.

3.3. The CCN Activation Properties of All-particles and BCc

3.3.1 Determining the D50 of BCc

279 The measurement of the activation properties of all-particles and BCc into CCN is discussed in Sec. 2.3.2. Figure
280 4 illustrates a representative example of size-resolved activation of all-particle and BCc at SS = 0.1% and 0.3%.
281 Activation commences for all-particles when [CCN] exceeds 0 (depicted by blue lines), while activation for BCc
282 (indicated by black lines) begins when the [CN_{unact}] (represent by green lines) falls below that of [BCc] (Fig. 4).
283 The [BC_{act}] (denoted by the grey shadow) can be derived using Equation 4, and the size-resolved $F_{act,BC}$ is
284 calculated accordance to Equation 5. It is observed that as particle size increase, BCc started to get activated at
285 0.19μm (0.13μm) at SS=0.1% (0.3%), which is higher than all-particle by 44% (46%). The higher D50 of BCc
286 also indicates that the lower κ_{BC} than κ_{all}.

287 We would like to emphasize that the principal uncertainty in the employed method arises from the assumption
288 that κ for BCc is lower compared to other particles. This assumption is consistent with current theoretical
289 understanding that pure BC is hydrophobic (κ_{BC}=0), although κ_{BC} increases by acquire hygroscopic coating
290 through atmospheric aging (Grimonprez et al., 2018; Weingartner et al., 1997), κ_{BC} remains lower than that of
291 other components under the same atmospheric oxidation process, based on ZSR volume mixing rule. Most
292 importantly, even though some internally mixing BCc activate into CCN prior to other chemical components, the
293 results here likely underestimated the [BC_{act}] and $F_{act,BC}$. Therefore, the CCN activity of BCc derived through this
294 method could represent the low bound of atmospheric BCc.

3.3.2 D50 of BCc and All-particles

296 Figure 5 illustrates the temporal evolution of the size distribution of BCc, CN and CCN, respectively. The [CCN]
297 increases during polluted conditions due to the increased concentration of BCc and all-particles, and the [CCN] is
298 mainly contributed by all-particles (Fig. 5c). The derived D50 for BCc and all-particles under water SS at 0.1%,
299 0.2%, and 0.3% is shown as lines in Fig. 5a-c for the temporal evolution, and the mean value is indicated by
300 vertical dash lines in Fig. 5d. The mean D50 of BCc (0.17μm, 0.13μm, and 0.12μm under SS= 0.1%, 0.2%, and
301 0.3%) was approximate 1.4 times larger than that of all-particles (0.11μm, 0.08μm, and 0.07μm under SS= 0.1%,
302 0.2%, and 0.3%) (Fig. 5), as expected from κ-Köhler theory (Petters and Kreidenweis, 2007) that lower/higher
303 D50 corresponds to higher/lower κ. The higher D50 of BCc also suggested a lower κ, indicating that BCc should
304 be activated in the last order.

305 Large variation of D50 of BCc and all-particles was also observed for different air masses (Fig. 5). The D50 of
306 all-particles (0.13μm ± 0.01μm) and BCc (0.20μm ± 0.01μm) during polluted C1 period was lower than (0.15μm
307 ± 0.02μm) and (0.23μm ± 0.02μm) during clean C3/C4 period. This is also inconsistent with the variation of κ_{all}
308 and κ_{BC} (discussed in 3.2), suggests the more inorganic fraction increase κ_{all} and the thick coating increase the κ_{BC}
309 during the polluted condition.

Figure 6a and 6b illustrate the diurnal variation of the D50 of all-particles and BCc under SS=0.10%, while the other two SSs at 0.20% and 0.30% are shown in Fig. S3 and Fig. S4. The diurnal variation was more pronounce under clean period (i.e. C3+C4), when local emissions dominated the pollution sources. Higher D50 of all-particles and BCc was found during the rush-hours when more primary hydrophobic OA and fresh external mixed BCc emitted. The D50 of all-particles and BCc will decrease after photochemistry oxidation secondary OA formation and coating on BCc, which was also consistent with the variation of κ_{all} and κ_{BC} (Fig. 3).

3.3.3 Droplet Activation Fraction of BCc and All-particles

Figure 5d shows the averaged size distribution of BCc, CN and CCN under three SSs for different periods classified by air mass clusters (C1-C4). Notably BCc had consistently larger peak size than all-particles for all air masses. For example, the BCc peak ranged from 185 to 210nm, approximately 2-4 times larger than that of all-particles, which peaked from 58 to 115nm. The more polluted air masses (C1 and C2) exhibited larger peak sizes for BCc and CN than the cleaner air masses (C3 and C4), because of the condensation process during polluted episodes when gases heavily partitioned into the aerosol phase and enlarged particle size.

Though the BC core size is smaller, after attaching on larger particles the overall coated size is even significantly larger than BCf. This suggests that in typical sub-urban environments, BC had been significantly associated with non-BC substances through condensation and coagulation process (Yu et al., 2022), and the bare BC without containing non-BC substance had taken a less proportion and most BCc had been enlarged during the aging process. This is consistent with previous studies that BC was associated with larger aerodynamic size than BCf (Pan et al., 2019; Wang et al., 2021). Previous studies also observed rapid aging of BC in a few hours in urban environment (Peng et al., 2016).

Figure 6d and 6e show the diurnal variations of F_{act} (in number and mass) for all-particles and BCc under SS=0.1%. The other two SSs at 0.2% and 0.3% are shown in Figure S2 and Figure S3. With SS increase from 0.1% to 0.2%, the number $F_{act,BC}$ and $F_{act,all}$ increased from 42%±15% to 69%±15% and from 30%±15% to 51%±19%. Figure 6f shows the statistical F_{act} results compared for different air masses, the number $F_{act,BC}$ increased from 30% to 53% under SS=0.1% (Fig. 6f) with the pollution increase from C3/C4 to C1. The mass $F_{act,BC}$ show similar variation characteristic as the number $F_{act,BC}$, increasing from 58% to 76% under SS=0.1% from C3/C4 to C1 period (Fig. 6f), and from 81% to 89% and from 87% to 91%, under SS at 0.2% and 0.3%, respectively. BCc acquires thicker hygroscopic coating through longer atmospheric aging time during the long-range regional transport in the polluted C1 period. The hygroscopic coating not only increases κ_{BC} and leads to a lower D50 but also increases BCc size. The decrease of D50 and increase of particle size both led to an increase of F_{act}. $F_{act,BC}$ mainly depended on the $V_{coating}/V_{BC}$, as the D50 and size of BCc are dependent on $V_{coating}/V_{BC}$. The diurnal variation also shows lowest $F_{act,BC}$ during rush hours due to lower $V_{coating}/V_{BC}$, and increases in the daytime with increased $V_{coating}/V_{BC}$ (Fig. 6e).

The number $F_{act,BC}$ was always higher than $F_{act,all}$ under all SSs (Fig. 6, Fig. S2 and Fig. S3) due to the larger size of BCc compare to all-particles. The mass $F_{act,BC}$ was about 1.61 times higher than in number, compared with about a 2.88 difference of mass and number F_{act} for all-particles. This is also caused by the larger size distribution of BCc than all-particle. The large portion of all-particles in small size drives the number F_{act} to be lower than BCc. Although D50 of BC is higher, the larger size distribution of BCc than all-particles means BCc can have a higher droplet removal efficiency than BCf.

The higher $F_{act,BC}$ than BCf particles and thickly coated BCc have preference in CCN activation was also observed through cloud residues observation at a mountain site in south China (Fu et al., 2022). The measured F_{act} was generally consistent with experiment conducted in a South China mega city using the same method (Hu et al., 2021a), but are higher than cloud residues observation in China (Zhang et al., 2017), which reported an average value 33% of the mass $F_{act,BC}$ and number F_{act} of BCc (all-particle) ranged in 5%-45% (7%-60%). We

attribute the difference to unknow ambient SS for the cloud, which have great influence on the $F_{act,BC}$. According to previous cloud residues observation at Jungfraujoch, the number $F_{act,BC}$ increase from 50% to 80% when SS increase from 0.21% to 0.50% (Motos et al., 2019a; Hammer et al., 2014). The ambient SS show large variation can be range from 0.01% to 2.00% (Hammer et al., 2014), however, it is challenging to directly observe the SS from field observation. Through this method, the number and mass $F_{act,BC}$ activated into droplets can be quantitatively investigate under certain ambient SS conditions, thus the results here provide a reference to investigate the lifetime of BCc.

3.4. Time Scale for the Evolution of CCN Activity of BCc

The temporal evolution of parameters related to CCN activity including κ, D50 and F_{act} against photochemical age (t_{age}) for BCc and all-particles are shown in Fig. 7. It demonstrates that the aging time (t_{ag}) can well explain the variation of all parameters for BCc and all-particles with a linear function ($R^2 > 0.4$).

The volume ratio of coating over rBC ($V_{coating}/V_{BC}$) showed an increase rate of 0.14 h^{-1} (Fig. S4), and can be fitted as:

$$V_{coating}/V_{BC} = 0.55 + 0.14 \cdot t_{age} \qquad (7)$$

This results in a linear increase rate for the hygroscopicity parameter, κ_{BC} showed a linear rate of 0.09 h^{-1} ((Fig. 7a, 7b, and 7c)) at all SSs, and can be fitted as:

$$\kappa_{BC} = 0.09 + 0.01 \cdot t_{age} \qquad (8)$$

In addition, κ_{BC} also follow a linear function with t_{age} as:

$$\kappa_{all} = 0.16 + 0.014 \cdot t_{age} \qquad (9)$$

This means the κ for the large proportion of non-BC is enhanced after aging due to enhanced formation of inorganic salt and secondary organic aerosols (Wu et al., 2022). The results show it will take about 24 and 10 hours to reach the global mean κ of 0.27-0.30 (Pringle et al., 2010) for BCc and all particles, respectively.

The aging scale of a few hours observed here is generally consistent with previously measured BC aging influenced by anthropogenic pollution, such as an aircraft measurement (Moteki et al., 2007) which observed the conversion time scale of BC to be a few hours under polluted environment. The results were also comparable with previous chamber studies that investigated the κ evolution of BC (Tritscher et al., 2011; Lambe et al., 2015; Peng et al., 2017), where the increase rate of κ_{BC} (0.01h^{-1}) in this study was similar, but the initial κ_{BC} here (0.08-0.26) was higher than that of fresh combustion soot as used in their results (0-0.12). These consistently showed a few hours tended to be a typical aging timescale to convert appreciable amount of initially hydrophobic BC to be hydrophilic, hereby CCN active. The exact timescale may vary according to pollution levels, such as a higher concentration of gas precursors and favoured meteorological condition may promote the growth rate of hygroscopic substances on BC.

Correspondingly, the D50 of BCc and all-particles decreased with t_{age}, with a rate of -3 nm h^{-1} and -3nm h^{-1}(Fig. 7d), -1 nm h^{-1} and -2nm h^{-1} (Fig. 7e), and -0.5 nm h^{-1} and -2 nm h^{-1} (Fig. 7f) under SS = 0.10%, 0.20%, and 0.30%, respectively. The results are summarized in Table 1.

The number activation fraction $F_{act,all}$ and $F_{act,BC}$ also showed linear corelation with t_{age}. A notable higher CCN activation fraction was observed for BCc than all particles at the same t_{age}, this was attributed to the larger coated size of BCc than other non-BC particles (Fig. 5). This difference between BCc and other particles was reduced at longer t_{age} because the sufficient aging time had allowed all particles to grow to similar large sizes.

After 8 hours of aging, $F_{act,BC}$ increased from 35% to 63% as SS rose from 0.1% to 0.2%, and then increase from

63% to 77% as SS increase from 0.2% to 0.3%. This illustrates a notable increase in $F_{act,BC}$ from SS=0.1% to 0.20%, but a less significantly changed $F_{act,BC}$ from SS=0.2% to 0.3%. Furthermore, the rate increase of $F_{act,BC}$ with t_{age} was 2% h^{-1} at SS=0.10% (Fig.7g), which was twice as large as at SS=0.2% (1% h^{-1}) (Fig. 7h) and 0.3% (1% h^{-1}) (Fig. 7i). This indicated that the activation of BCc was more sensitive at lower SS (<0.2%), but may reach a plateau when SS>0.2%. This is because the activation diameter at this typical SS range was close to the mode size of BCc number distribution (Fig. 5d), and a small increase of SS will cause a considerable change of fraction which is larger than the activation diameter. The SS range from 0.1% to 0.2% is for the typical formation of fog and stratiform thin clouds (Hammer et al., 2014).

4. Conclusion

In this study, we conducted directly measurements of the droplet activation of BC-containing particles under water supersaturation conditions in a suburban environment. Both the hygroscopicity and CCN activation diameters reveal that the hygroscopicity of all-particles and BCc concurrently increases with polluted levels, primarily governed by the amount of coating. As pollution intensifies, the volume ratio of coating over rBC increases from 1.8 to 4.7, causing the hygroscopicity of BCc to increases from 0.11 to 0.23. The increase of coating not only increase BCc's hygroscopicity but also shifts these particles to larger sizes, significantly enhance their CCN activity. The number activated fraction of BCc was 42% under SS at 0.1%, higher than the 30% activation of all particles. Despite the lower hygroscopicity, the elevated activation fraction of BCc can be attributed to their larger size compared to all particles. It was also found that the number activated fraction of BCc was more sensitive in the SS range from 0.1% to 0.2% (Hu et al., 2021a), a typical range for fog and stratiform thin clouds formation. This indicates a small increase of SS even for the environment with relatively low moisture and weak updraft the BC can be activated. Considering these clouds have a lower precipitation rate, BC in these clouds may have more persistent indirect radiative impacts.

Furthermore, we successfully parameterized the evolution of hygroscopicity and CCN activation characteristics of BCc and all particles in relation to equivalent photochemical age. The hygroscopicity of BCc was found positive linearly correlated with aging time with a rate of 0.01 h^{-1}, and the activation diameter negative correlated with a rate of 1-3 nm h^{-1}. Within 10 hours, 65% of BCc activated under SS=0.2% in this typical sub-urban environment, this is in line with a wide range of recent ambient studies that BC can be half activated under SS=0.1-0.2%. This means these BCc may be efficiently incorporated into clouds by serving as CCN. This aging process by acquiring more hygroscopic substances of BC may be particularly important under polluted environment, where the condensation and coagulation processes intensively occurred. The results here thus provide direct evidence of efficient droplet activation of BCc, and the aging scale associated with their CCN activation can be used as a refence to validate the regional models regarding aerosol-cloud interactions of BC.

Competing interests. At least one of the (co-)authors is a member of the editorial board of Atmospheric Chemistry and Physics.

Author contribution. D. D., and M. H. led and designed the study; P. T. and D. L. designed the study, set up the experiment, analysed the data, and wrote the paper. K. H. and Y. W. conducted the field observation and contributed the data analysis. H. H. and J. S performed the calibration of the instruments. C. Y. and D. H contributed to scientific discussion.

435

Reference

Bond, T. C., Doherty, S. J., Fahey, D. W., Forster, P. M., Berntsen, T., DeAngelo, B. J., Flanner, M. G., Ghan, S., Kärcher, B., Koch, D., Kinne, S., Kondo, Y., Quinn, P. K., Sarofim, M. C., Schultz, M. G., Schulz, M., Venkataraman, C., Zhang, H., Zhang, S., Bellouin, N., Guttikunda, S. K., Hopke, P. K., Jacobson, M. Z., Kaiser, J. W., Klimont, Z., Lohmann, U., Schwarz, J. P., Shindell, D., Storelvmo, T., Warren, S. G., and Zender, C. S.: Bounding the role of black carbon in the climate system: A scientific assessment, J. Geophys. Res. Atmos., 118, 11, 5380-5552, 2013.

Bruns, E. A., El Haddad, I., Slowik, J. G., Kilic, D., Klein, F., Baltensperger, U., and Prevot, A. S.: Identification of significant precursor gases of secondary organic aerosols from residential wood combustion, Sci. Rep., 6, 27881, 2016.

Cui, S., Huang, D. D., Wu, Y., Wang, J., Shen, F., Xian, J., Zhang, Y., Wang, H., Huang, C., Liao, H., and Ge, X.: Chemical properties, sources and size-resolved hygroscopicity of submicron black-carbon-containing aerosols in urban Shanghai, Atmos. Chem. Phys., 22, 8073-8096, 2022.

Dalirian, M., Ylisirniö, A., Buchholz, A., Schlesinger, D., Ström, J., Virtanen, A., and Riipinen, I.: Cloud droplet activation of black carbon particles coated with organic compounds of varying solubility, Atmos. Chem. Phys., 18, 12477-12489, 2018.

Deng, Z. Z., Zhao, C. S., Ma, N., Liu, P. F., Ran, L., Xu, W. Y., Chen, J., Liang, Z., Liang, S., Huang, M. Y., Ma, X. C., Zhang, Q., Quan, J. N., Yan, P., Henning, S., Mildenberger, K., Sommerhage, E., Schäfer, M., Stratmann, F., and Wiedensohler, A.: Size-resolved and bulk activation properties of aerosols in the North China Plain, Atmos. Chem. Phys., 11, 3835-3846, 2011.

Draxier, R. R., & Hess, G. D.: An overview of the HYSPLIT4 modelling system for trajectories, dispersion, and deposition, Australian Meteorological Magazine, 47, 4, 295–308, 1998.

Drewnick, F., Hings, S. S., DeCarlo, P., Jayne, J. T., Gonin, M., Fuhrer, K., Weimer, S., Jimenez, J. L., Demerjian, K. L., Borrmann, S., and Worsnop, D. R.: A New Time-of-Flight Aerosol Mass Spectrometer (TOF-AMS)—Instrument Description and First Field Deployment, Aerosol Sci. Technol., 39, 637-658, 2005.

Dusek, U., Reischl, G. P., and Hitzenberger, R.: CCN activaton of pure and coated carbon black particles, Environ. Sci. Technol., 40, 1223-1230, 2006.

Friebel, F., Lobo, P., Neubauer, D., Lohmann, U., Drossaart van Dusseldorp, S., Mühlhofer, E., and Mensah, A. A.: Impact of isolated atmospheric aging processes on the cloud condensation nuclei activation of soot particles, Atmos. Chem. Phys., 19, 15545-15567, 2019.

Fu, Y., Peng, X., Sun, W., Hu, X., Wang, D., Yang, Y., Guo, Z., Wang, Y., Zhang, G., Zhu, J., Ou, J., Shi, Z., Wang, X., and Bi, X.: Impact of Cloud Process in the Mixing State and Microphysical Properties of Soot Particles: Implications in Light Absorption Enhancement, J. Geophys. Res. Atmos., 127, 2022.

Gao, R. S., Schwarz, J. P., Kelly, K. K., Fahey, D. W., Watts, L. A., Thompson, T. L., Spackman, J. R., Slowik, J. G., Cross, E. S., Han, J. H., Davidovits, P., Onasch, T. B., and Worsnop, D. R.: A Novel Method for Estimating Light-Scattering Properties of Soot Aerosols Using a Modified Single-Particle Soot Photometer, Aerosol Sci. Technol., 41, 125-135, 2007.

Grimonprez, S., Faccinetto, A., Batut, S., Wu, J., Desgroux, P., and Petitprez, D.: Cloud condensation nuclei from the activation with ozone of soot particles sampled from a kerosene diffusion flame, Aerosol Sci. Technol., 52, 814-827, 2018.

Hammer, E., Bukowiecki, N., Gysel, M., Jurányi, Z., Hoyle, C. R., Vogt, R., Baltensperger, U., and Weingartner, E.: Investigation of the effective peak supersaturation for liquid-phase clouds at the high-alpine site Jungfraujoch, Switzerland (3580 m a.s.l.), Atmos. Chem. Phys., 14, 1123-1139, 2014.

Hansen, J., Sato, M., and Ruedy, R.: Radiative forcing and climate response, J. Geophys. Res. Atmos., 102, 6831-6864, 1997.

Henning, S., Ziese, M., Kiselev, A., Saathoff, H., Möhler, O., Mentel, T. F., Buchholz, A., Spindler, C., Michaud,

V., Monier, M., Sellegri, K., and Stratmann, F.: Hygroscopic growth and droplet activation of soot particles: uncoated, succinic or sulfuric acid coated, Atmos. Chem. Phys., 12, 4525-4537, 2012.

Henning, S., Wex, H., Hennig, T., Kiselev, A., Snider, J. R., Rose, D., Dusek, U., Frank, G. P., Pöschl, U., Kristensson, A., Bilde, M., Tillmann, R., Kiendler-Scharr, A., Mentel, T. F., Walter, S., Schneider, J., Wennrich, C., and Stratmann, F.: Soluble mass, hygroscopic growth, and droplet activation of coated soot particles during LACIS Experiment in November (LExNo), J. Geophys. Res. Atmos., 115, D11206, 2010.

Hu, D., Liu, D., Kong, S., Zhao, D., Wu, Y., Li, S., Ding, S., Zheng, S., Cheng, Y., Hu, K., Deng, Z., Wu, Y., Tian, P., Liu, Q., Huang, M., and Ding, D.: Direct Quantification of Droplet Activation of Ambient Black Carbon Under Water Supersaturation, J. Geophys. Res. Atmos., 126, e2021JD034649, 2021a.

Hu, K., Liu, D., Tian, P., Wu, Y., Deng, Z., Wu, Y., Zhao, D., Li, R., Sheng, J., Huang, M., Ding, D., Li, W., Wang, Y., and Wu, Y.: Measurements of the Diversity of Shape and Mixing State for Ambient Black Carbon Particles, Geophys. Res. Lett., 48, e2021GL094522, 2021b.

Hu, K., Liu, D., Tian, P., Wu, Y., Li, S., Zhao, D., Li, R., Sheng, J., Huang, M., Ding, D., Liu, Q., Jiang, X., Li, Q., and Tao, J.: Identifying the Fraction of Core–Shell Black Carbon Particles in a Complex Mixture to Constrain the Absorption Enhancement by Coatings, Environ. Sci. Technol., 9, 272-279, 2022.

Jacobson, M. Z.: Short-term effects of controlling fossil-fuel soot, biofuel soot and gases, and methane on climate, Arctic ice, and air pollution health, J. Geophys. Res., 115, D14209, 2010.

Jayne, J. T., Leard, D. C., Zhang, X., Davidovits, P., Smith, K. A., Kolb, C. E., and Worsnop, D. R.: Development of an Aerosol Mass Spectrometer for Size and Composition Analysis of Submicron Particles, Aerosol Sci. Technol., 33, 49-70, 2000.

Knutson, E. O. and Whitby, K. T.: Aerosol classification by electric mobility: Apparatus, Theory, and Applications, Aerosol Sci., 6, 443, 1975.

Koch, D. and Del Genio, A. D.: Black carbon semi-direct effects on cloud cover: review and synthesis, Atmos. Chem. Phys., 10, 7685-7696, 2010.

Koch, D., Balkanski, Y., Bauer, S. E., Easter, R. C., Ferrachat, S., Ghan, S. J., Hoose, C., Iversen, T., Kirkevåg, A., Kristjansson, J. E., Liu, X., Lohmann, U., Menon, S., Quaas, J., Schulz, M., Seland, Ø., Takemura, T., and Yan, N.: Soot microphysical effects on liquid clouds, a multi-model investigation, Atmos. Chem. Phys., 11, 1051-1064, 2011.

Koch, D., Schulz, M., Kinne, S., McNaughton, C., Spackman, J. R., Balkanski, Y., Bauer, S., Berntsen, T., Bond, T., Boucher, O., Chin, M., Clarke, A., Luca, N. D., Dentener, F., Diehl, T., Dubovik, O., Easter, R., Fahey, D. W., Feichter, J., Fillmore, D., Freitag, S., Ghan, S., Ginoux, P., Gong, S., Horowitz, L., Iversen, T., Kirkevåg, A., Kilmont, Z., Kondo, Y., Krol, M., Liu, X., Miller, R., Montanaro, V., Moteki, N., Myhre, G., Penner, J. E., Perlwiz, J., Pitari, G., Reddy, S., Sahu, L., Sakamoto, H., Schuster, G., Schwarz, J. P., Seland, Ø., Siter, P., Takegawa, N., Takemura, T., Textor, C., van Aardenne, J. A., and Zhao, Y.: Evaluation of black carbon estimations in global aerosol models, Atmos. Chem. Phys., 9, 9001-9026, 2009.

Kondo, Y., Moteki, N., Oshima, N., Ohata, S., Koike, M., Shibano, Y., Takegawa, N., and Kita, K.: Effects of wet deposition on the abundance and size distribution of black carbon in East Asia, J. Geophys. Res. Atmos., 121, 4691-4712, 2016.

Kuwata, M., Kondo, Y., Mochida, M., Takegawa, N., and Kawamura, K.: Dependence of CCN activity of less volatile particles on the amount of coating observed in Tokyo, J. Geophys. Res. Atmos., 112, D11207, 2007.

Laborde, M., Mertes, P., Zieger, P., Dommen, J., Baltensperger, U., and Gysel, M.: Sensitivity of the Single Particle Soot Photometer to different black carbon types, Atmos. Meas. Tech., 5, 1031-1043, 2012.

Lambe, A. T., Ahern, A. T., Wright, J. P., Croasdale, D. R., Davidovits, P., and Onasch, T. B.: Oxidative aging and cloud condensation nuclei activation of laboratory combustion soot, J. Aerosol Res. Atmos., 79, 31-39, 2015.

Liu, D., Allan, J., Whitehead, J., Young, D., Flynn, M., Coe, H., McFiggans, G., Fleming, Z. L., and Bandy, B.: Ambient black carbon particle hygroscopic properties controlled by mixing state and composition, Atmos. Chem.

Phys., 13, 2015-2029, 2013.

Liu, D., Allan, J. D., Young, D. E., Coe, H., Beddows, D., Fleming, Z. L., Flynn, M. J., Gallagher, M. W., Harrison, R. M., Lee, J., Prevot, A. S. H., Taylor, J. W., Yin, J., Williams, P. I., and Zotter, P.: Size distribution, mixing state and source apportionment of black carbon aerosol in London during wintertime, Atmos. Chem. Phys., 14, 10061-10084, 2014.

Liu, D., Ding, S., Zhao, D., Hu, K., Yu, C., Hu, D., Wu, Y., Zhou, C., Tian, P., Liu, Q., Wu, Y., Zhang, J., Kong, S., Huang, M., and Ding, D.: Black Carbon Emission and Wet Scavenging From Surface to the Top of Boundary Layer Over Beijing Region, J. Geophys. Res. Atmos., 125, e2020JD033096, 2020.

Liu, D., Whitehead, J., Alfarra, M. R., Reyes-Villegas, E., Spracklen, Dominick V., Reddington, Carly L., Kong, S., Williams, Paul I., Ting, Y.-C., Haslett, S., Taylor, Jonathan W., Flynn, Michael J., Morgan, William T., McFiggans, G., Coe, H., and Allan, James D.: Black-carbon absorption enhancement in the atmosphere determined by particle mixing state, Nat. Geosci., 10, 184-188, 2017.

Liu, J., Chu, B. W., Chen, T. Z., Liu, C. G., Wang, L., Bao, X. L., He, H.: Secondary organic aerosol formation from ambient air at an urban site in Beijing: Effects of OH exposure and precursor concentrations, Environ. Sci. Technol., 52, 12, 6834-6841, 2018.

Lund, M. T., Berntsen, T. K., and Samset, B. H.: Sensitivity of black carbon concentrations and climate impact to aging and scavenging in OsloCTM2–M7, Atmos. Chem. Phys., 17, 6003-6022, 2017.

McDonald, J. E.: Erroneous Cloud-Physics Applications of Raoult's Law, J. Meteorol., 10, 68-70, 1953.

Middlebrook, A. M., Bahreini, R., Jimenez, J. L., and Canagaratna, M. R.: Evaluation of Composition-Dependent Collection Efficiencies for the Aerodyne Aerosol Mass Spectrometer using Field Data, Aerosol Sci. Technol., 46, 258-271, 2012.

Moore, R. H., Nenes, A., and Medina, J.: Scanning Mobility CCN Analysis—A Method for Fast Measurements of Size-Resolved CCN Distributions and Activation Kinetics, Aerosol Sci. Technol., 44, 861-871, 2010.

Moteki, N., Kondo, Y., Miyazaki, Y., Takegawa, N., Komazaki, Y., Kurata, G., Shirai T., Blake, D. R., Miyakawa, T., Koike, M.: Evolution of mixing state of black carbon particles: aircraft measurements over the western pacific in march 2004. Geophysical Research Letters, 34(11), 235-255, 2007.

Moteki, N., Kondo, Y., and Nakamura, S.-i.: Method to measure refractive indices of small nonspherical particles: Application to black carbon particles, J. Aerosol Res. Atmos., 41, 513-521, 2010.

Motos, G., Schmale, J., Corbin, J. C., Zanatta, M., Baltensperger, U., and Gysel-Beer, M.: Droplet activation behaviour of atmospheric black carbon particles in fog as a function of their size and mixing state, Atmos. Chem. Phys., 19, 2183-2207, 2019a.

Motos, G., Schmale, J., Corbin, J. C., Modini, R. L., Karlen, N., Bertò, M., Baltensperger, U., and Gysel-Beer, M.: Cloud droplet activation properties and scavenged fraction of black carbon in liquid-phase clouds at the high-alpine research station Jungfraujoch (3580 m a.s.l.), Atmos. Chem. Phys., 19, 3833-3855, 2019b.

Ohata, S., Schwarz, J. P., Moteki, N., Koike, M., Takami, A., Kondo, Y.: Hygroscopicity of materials internally mixed with black carbon measured in Tokyo, J. Geophys. Res. Atmos., 121, 362-381, 2016.

Onasch, T. B., Trimborn, A., Fortner, E. C., Jayne, J. T., Kok, G. L., Williams, L. R., Davidovits, P., and Worsnop, D. R.: Soot Particle Aerosol Mass Spectrometer: Development, Validation, and Initial Application, Aerosol Sci. Technol., 46, 804-817, 2012.

Pan, X., Liu, H., Wu, Y., Tian, Y., Sun, Y., Xie, C., Liu, X., Cheng, T., and Wang, Z.: Dynamic shape factor and mixing state of refractory black carbon particles in winter in Beijing using an AAC-DMA-SP2 tandem system, Atmos. Chem. Phys. Discuss, 10.5194/acp-2019-433, 2019.

Parrish, D. D., Stohl, A., Forster, C., Atlas, E. L., Blake, D. R., Goldan, P. D., Kuster, W. C., Gouw, J. A. de.: Effects of mixing on evolution of hydrocarbon ratios in the troposphere, J. Geophys. Res. Atmos., 112, D10S34, 2007.

Park, R. J., Jacob, D. J., Palmer, P. I., Clarke, A. D., Weber, R. J., Zondlo, M. A., Eisele, F. L., Bandy, A. R.,

Thornton, D. C., Sachse, G. W., and Bond, T. C.: Export efficiency of black carbon aerosol in continental outflow: Global implications, J. Geophys. Res. Atmos., 110, D11205,2005.

Peng, J., Hu, M., Guo, S., Du, Z., Shang, D., Zheng, J., Zheng, J., Zeng, L., Shao, M., Wu, Y., Collins, D., and Zhang, R.: Ageing and hygroscopicity variation of black carbon particles in Beijing measured by a quasi-atmospheric aerosol evolution study (QUALITY) chamber, Atmos. Chem. Phys., 17, 10333-10348, 2017.

Peng, J., Hu, M., Guo, S., Du, Z., Zheng, J., Shang, D., Zamora, M. L., Zeng, L., Shao, M., Wu, Y., Zheng, j., Wang, Y., Glen, C. R., Collins, D., Molina, M. J., and Zhang, R.: Markedly enhanced absorption and direct radiative forcing of black carbon under polluted urban environments, Proc. Natl. Acad. Sci. U S A, 113, 4266-4271, 2016.

Petters, M. D. and Kreidenweis, S. M.: A single parameter representation of hygroscopic growth and cloud condensation nucleus activity, Atmos. Chem. Phys., 7, 1961-1971, 2007.

Pringle, K. J., Tost, H., Pozzer, A., Pöschl, U., and Lelieveld, J.: Global distribution of the effective aerosol hygroscopicity parameter for CCN activation, Atmos. Chem. Phys., 10, 5241-5255, 2010.

Pruppacher, H. R. and Klett, J. D.: Microphysics of Cloud and Precipitation, Kluwer Academic Publishers, Dordrecht,1997.

Ramanathan, V. and Carmichael, G.: Global and regional climate changes due to black carbon, Nat. Geosci., 1, 221-227, 2008.

Roberts, G. C. and Nenes, A.: A Continuous-Flow Streamwise Thermal-Gradient CCN Chamber for Atmospheric Measurements, Aerosol Sci. Technol., 39, 206-221, 2005.

Rose, D., Gunthe, S. S., Mikhailov, E., Frank, G. P., Dusek, U., Andreae, M. O., and Pöschl, U.: Calibration and measurement uncertainties of a continuous-flow cloud condensation nuclei counter (DMT-CCNC): CCN activation of ammonium sulfate and sodium chloride aerosol particles in theory and experiment, Atmos. Chem. Phys., 8, 1153-1179, 2008.

Rose, D., Gunthe, S. S., Su, H., Garland, R. M., Yang, H., Berghof, M., Cheng, Y. F., Wehner, B., Achtert, P., Nowak, A., Wiedensohler, A., Takegawa, N., Kondo, Y., Hu, M., Zhang, Y., Andreae, M. O., and Pöschl, U.: Cloud condensation nuclei in polluted air and biomass burning smoke near the mega-city Guangzhou, China – Part 2: Size-resolved aerosol chemical composition, diurnal cycles, and externally mixed weakly CCN-active soot particles, Atmos. Chem. Phys., 11, 2817-2836, 2011.

Snider, J. R., Wex, H., Rose, D., Kristensson, A., Stratmann, F., Hennig, T., Henning, S., Kiselev, A., Bilde, M., Burkhart, M., Dusek, U., Frank, G. P., Kiendler-Scharr, A., Mentel, T. F., Petters, M. D., and Pöschl, U.: Intercomparison of cloud condensation nuclei and hygroscopic fraction measurements: Coated soot particles investigated during the LACIS Experiment in November (LExNo), J. Geophys. Res. Atmos., 115, D11205,2010.

Tian, P., Liu, D., Zhao, D., Yu, C., Liu, Q., Huang, M., Deng, Z., Ran, L., Wu, Y., Ding, S., Hu, K., Zhao, G., Zhao, C., and Ding, D.: In situ vertical characteristics of optical properties and heating rates of aerosol over Beijing, Atmos. Chem. Phys., 20, 2603-2622, 2020.

Tian, P., Liu, D., Bi, K., Huang, M., Wu, Y., Hu, K., Li, R., He, H., Ding, D., Hu, Y., Liu, Q., Zhao, D., Qiu, Y., Kong, S., and Xue, H.: Evidence for Anthropogenic Organic Aerosols Contributing to Ice Nucleation, Geophys. Res. Lett., 49, e2022GL099990, 2022.

Tritscher, T., Jurányi, Z., Martin, M., Chirico, R., Gysel, M., Heringa, M. F., DeCarlo, P. F., Sierau, B., Prévôt, A. S. H., Weingartner, E., and Baltensperger, U.: Changes of hygroscopicity and morphology during ageing of diesel soot, Environ. Res. Lett., 6, 034026, 2011.

Wang, J., Ye, J., Liu, D., Wu, Y., Zhao, J., Xu, W., Xie, C., Shen, F., Zhang, J., Ohno, P. E., Qin, Y., Zhao, X., Martin, S. T., Lee, A. K. Y., Fu, P., Jacob, D. J., Zhang, Q., Sun, Y., Chen, M., and Ge, X.: Characterization of submicron organic particles in Beijing during summertime: comparison between SP-AMS and HR-AMS, Atmos. Chem. Phys., 20, 14091–14102, 2020.

Wang, S., Zhou, K., Lu, X., Chen, H., Yang, F., Li, Q., Yang, X., and Wang, X.: Measurement of Density and

Shape for Single Black Carbon Aerosols in a Heavily Polluted Urban Area, Aerosol. Air. Qual. Res., 21, 210162, 2021.

Weingartner, E., Baltensperger, U., and Burtscher, H.: Growth and Structural Change of Combustion Aerosols at High Relative Humidity, Environ. Sci. Technol., 29, 2982-2986, 1995.

Weingartner, E., Burtscher, H., and Baltensperger, U.: Hygroscopic properties of carbon and diesel soot particles, Atmos. Environ., 31, 2311-2327, 1997.

Wiedensohler, A.: An approximation of the bipolar charge distribution for particles in the submicron size range, J. Aerosol Sci., 19, 387-389, 1988.

Wu, Y., Liu, D., Wang, J., Shen, F., Chen, Y., Cui, S., Ge, S., Wu, Y., Chen, M., and Ge, X.: Characterization of Size-Resolved Hygroscopicity of Black Carbon-Containing Particle in Urban Environment, Environ. Sci. Technol., 53, 14212-14221, 2019.

Wu, Y., Liu, D., Tian, P., Sheng, J., Liu, Q., Li, R., Hu, K., Jiang, X., Li, S., Bi, K., Zhao, D., Huang, M., Ding, D., and Wang, J.: Tracing the Formation of Secondary Aerosols Influenced by Solar Radiation and Relative Humidity in Suburban Environment, J. Geophys. Res. Atmos., 127, e2022JD036913, 2022.

Yu, C., Liu, D., Hu, K., Tian, P., Wu, Y., Zhao, D., Wu, H., Hu, D., Guo, W., Li, Q., Huang, M., Ding, D., and Allan, J. D.: Aerodynamic size-resolved composition and cloud condensation nuclei properties of aerosols in a Beijing suburban region, Atmos. Chem. Phys., 22, 4375-4391, 2022.

Yuan, B., Shao, M., de Gouw, J., Parrish, D. D., Lu, S., Wang, M., Zeng, L., Zhang, Q., Song, Y., Zhang, J., and Hu, M.: Volatile organic compounds (VOCs) in urban air: How chemistry affects the interpretation of positive matrix factorization (PMF) analysis, J. Geophys. Res. Atmos., 117, D24302, 2012.

Zhang, G., Lin, Q., Peng, L., Bi, X., Chen, D., Li, M., Li, L., Brechtel, F. J., Chen, J., Yan, W., Wang, X., Peng, P., amp, apos, an, Sheng, G., and Zhou, Z.: The single-particle mixing state and cloud scavenging of black carbon: a case study at a high-altitude mountain site in southern China, Atmos. Chem. Phys., 17, 14975-14985, 10.5194/acp-17-14975-2017, 2017.

Zhang, R., Khalizov, A. F., Pagels, J., Zhang, D., Xue, H., and McMurry, P. H.: Variability in morphology, hygroscopicity, and optical properties of soot aerosols during atmospheric processing, Proc. Natl. Acad. Sci. USA, 105, 10291-10296, 2008.

Zhao, D., Liu, D., Yu, C., Tian, P., Hu, D., Zhou, W., Ding, S., Hu, K., Sun, Z., Huang, M., Huang, Y., Yang, Y., Wang, F., Sheng, J., Liu, Q., Kong, S., Li, X., He, H., and Ding, D.: Vertical evolution of black carbon characteristics and heating rate during a haze event in Beijing winter, Sci.Total Environ., 709, 136251, 2020.

651 Table 1. A summary of linear fitting results for activation diameter (D50) and activation fraction (F_{act}) of all
652 particles and BCc-containing particles.
653

Initial, Slope	Activation diameter (D50)		Activation fraction (F_{act})	
	All particles	BC-containing particles	All particles	BC-containing particles
SS=0.1%	170nm, -3nm h^{-1}	240nm, -3nm h^{-1}	4%, 2% h^{-1}	19%, 2% h^{-1}
SS=0.2%	120nm, -2nm h^{-1}	170nm, -1nm h^{-1}	18%, 0.3%h^{-1}	55%, 0.1% h^{-1}
SS=0.3%	100nm, -2nm h^{-1}	150nm, -0.5nm h^{-1}	26%, 0.3% h^{1}	69%, 0.1% h^{-1}

654

Figures and captions
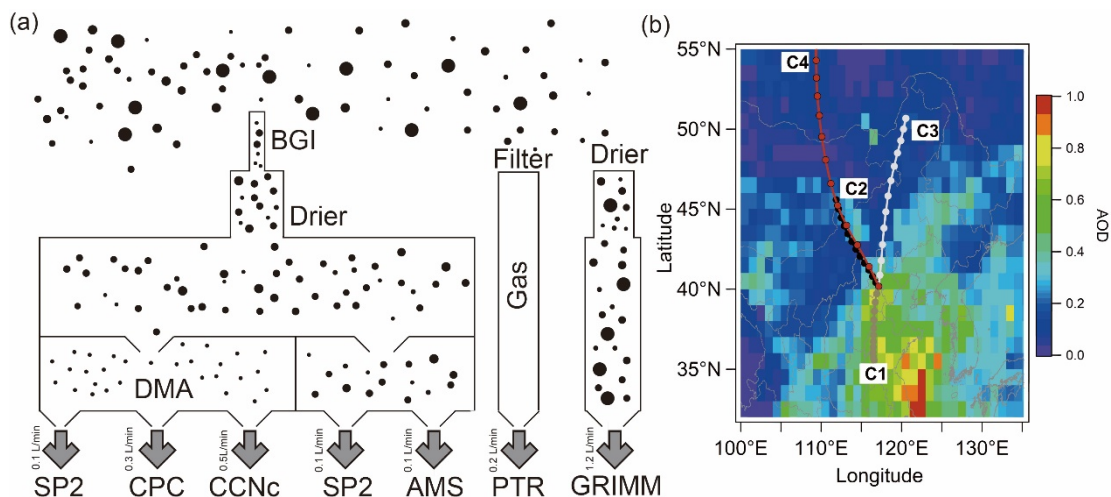
Figure 1. Schematic of the experiment. a) Experimental setup showing aerosols are sampled through a $PM_{2.5}$ impactor following a drier. Mono-dispersed aerosol was measured downstream of a differential mobility analyser (DMA), including SP2, CPC and CCNc, and additional line measure the poly-dispersed aerosols with SP2 and HR-ToF-AMS. All sizes of dried aerosol are measured by a GRIMM, and the VOC concentration was measured by a PTR-TOF-AMS. b) Mean aerosol optical depth (AOD) during the experimental month, with three lines showing the clustered 36h backward trajectories initialized from the experimental site with each markers denoting 6h transport time.
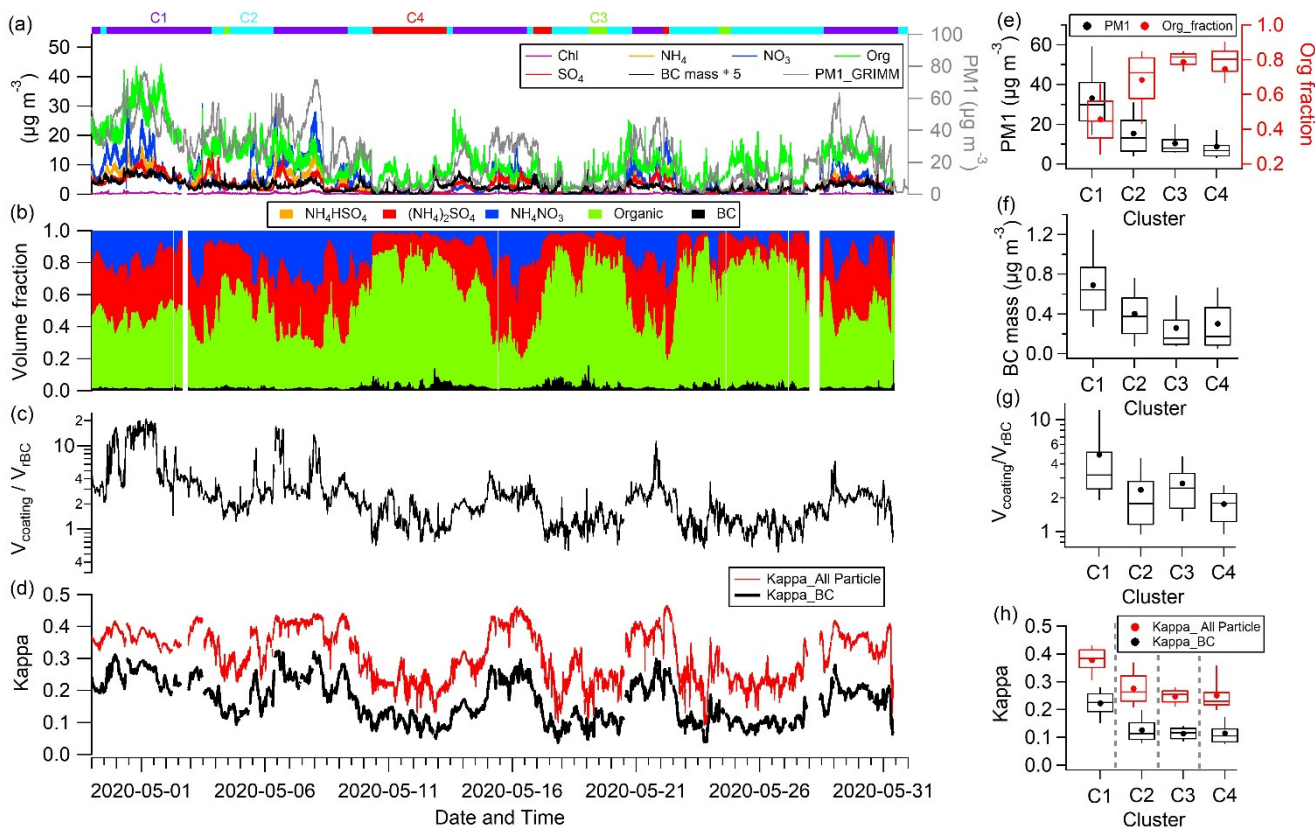
Figure 2. Time series of a) mass concentrations for chloride (Chl), ammonium (NH_4), nitrate (NO_3^-), organic (Org), sulfate (SO_4^{2-}), BC mass and PM_1 measured by HR-TOF-AMS, SP2 and GRIMM. b) Volume fraction of particle components for NH_4HSO_4, $(NH_4)_2SO_4$, NH_4NO_3, Organic and BC, c) $V_{coating}/V_{BC}$, d) κ for all particle and BC respectively. The flag on the top of the graph represents different clusters by different colours. Mass concentrations of e) Organic fraction and PM1 by summing HR-ToF-AMS components and BC mass from SP2, f) BC mass, g) $V_{coating}/V_{BC}$, h) κ, i) t_{age} for all particle (red) and BC (black) for four clusters, with solid circle indicating the average; in each box, the solid line and top and bottom boundaries represent the median, 75th and 25th percentiles, respectively.
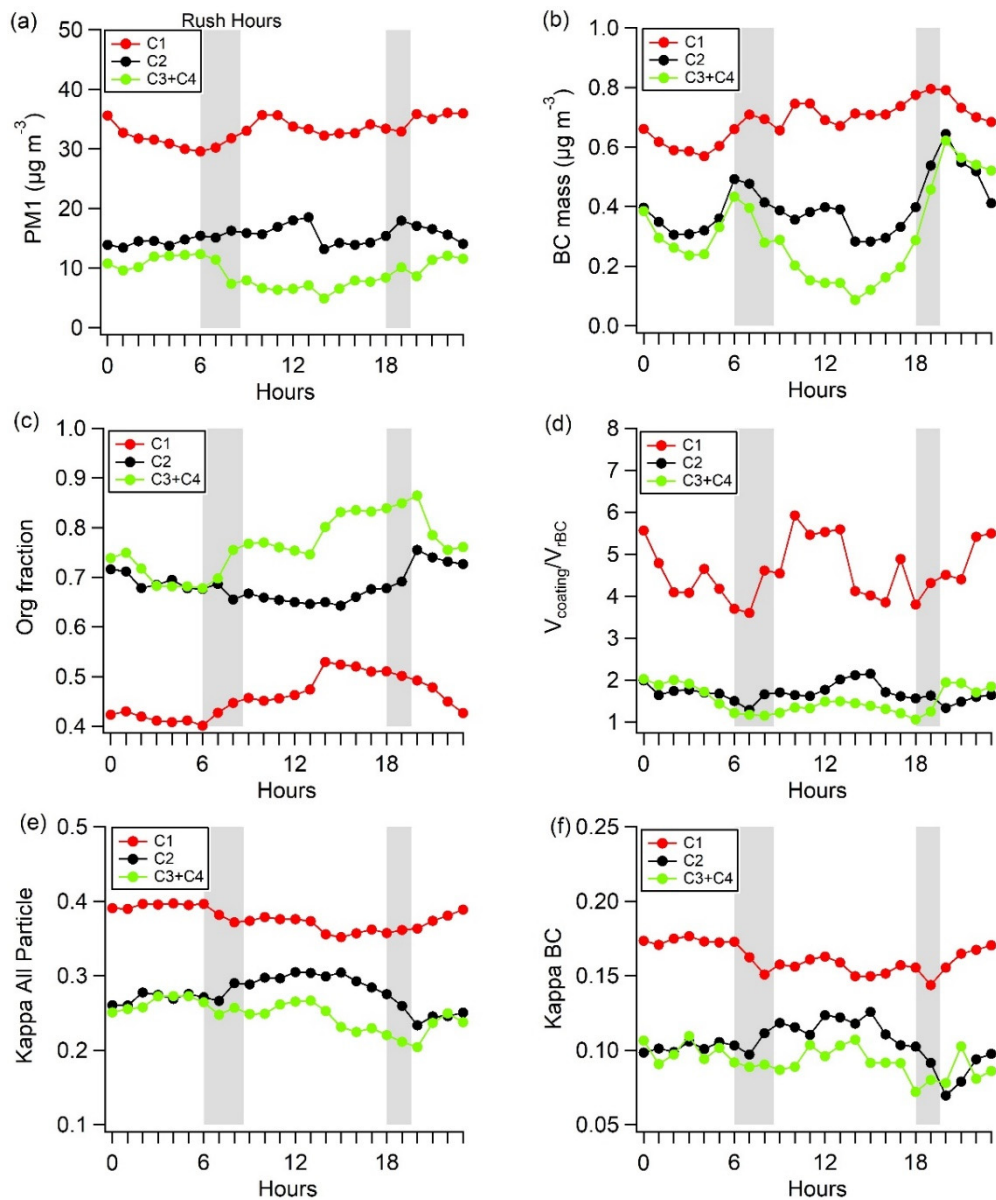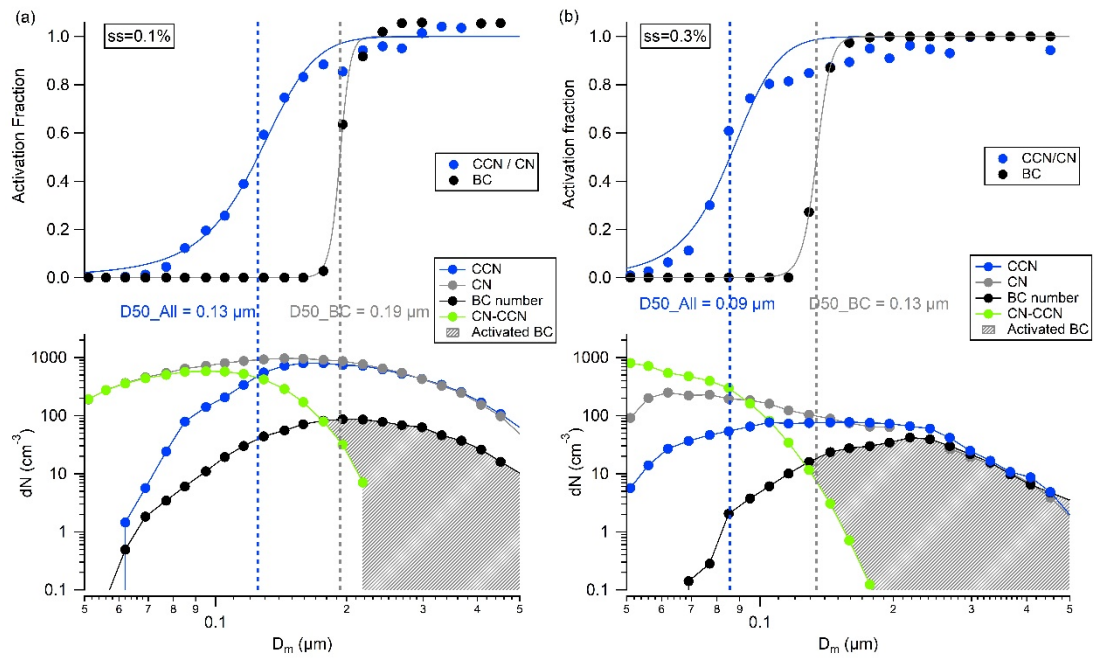
Figure 3. Diurnal variations of a) PM_1, b) BC mass, c) Organic fraction, d) $V_{coating}/V_{BC}$, e) κ for all particles and f) κ for BC for four clusters, respectively. Grey bars indicate the traffic rush hours, and the red, black, and green line represent the C1, C2 and C3/C4 period, respectively.

**Figure 4**. A typical example of size-resolved number concentrations of CN, CCN and BCc under supersaturation of a) 0.1% and b) 0.3%. The green lines show the un-activated number concentration and the grey shadows indicate the activated BCc number concentrations at each size. The blue and black dots in the upper panel show the activation fraction of all-particle and BCc. The blue and grey lines indicate the sigmoid fitting on the size-resolved activation fraction of all-particle and BC respectively, with the vertical dash lines indicating the respective activation diameters.
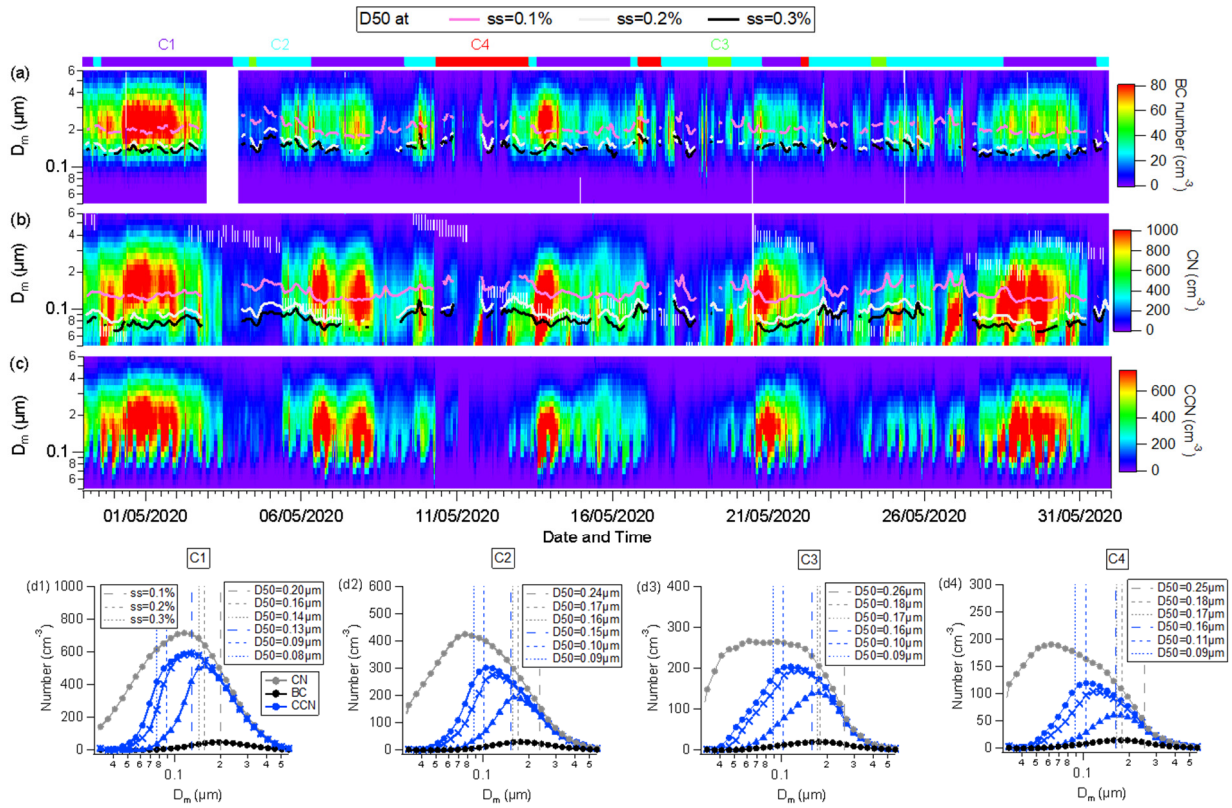
**Figure 5.** Temporal evolution of numbers of a) BCc, b) CN, c) CCN and activation diameter (D50) of BCc and CN particles under SS=0.1%, 0.2% and 0.3%. d) Mobility particles size distribution of CN, BCc and CCN numbers under SS=0.1%, 0.2% and 0.3% for different clusters. The blue and grey dash lines on the images denote the D50 for all-particles and BCc under different SS, respectively. Bottom panels show the mean particles size distributions of CN, CCN (under the three SSs) and BCc, for the classified air masses.
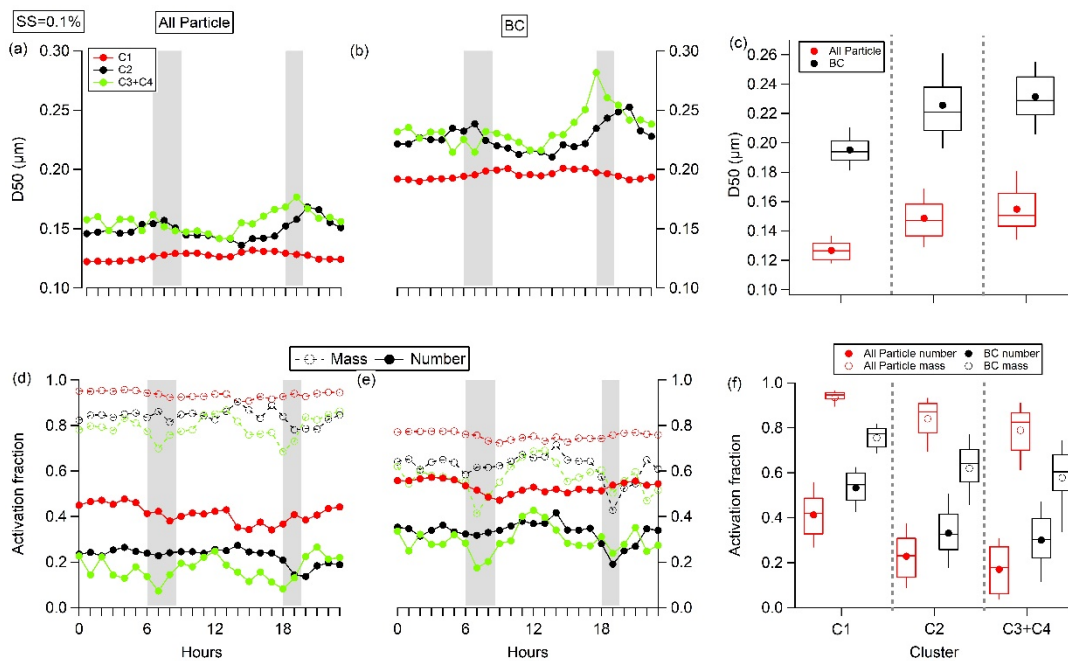
Figure 6. Diurnal variations of D50 of a) all-particles, and b) BCc particles under SS=0.1% for different air mass clusters, respectively, c) the statistical of D50 for different air mass cluster, with solid circle indicating the average; in each box, the solid line and top and bottom boundaries represent the median, 75th and 25th, respectively. c) diurnal variation of the activation fraction of all-particles, and e) BCc particles, with the solid and dash line represent the number and mass fraction, the mass (number) activation fraction was calculated by summing the mass (number) of particles with diameter larger than D50, and divided by the total mass (number). f) statistical of the activation fraction.
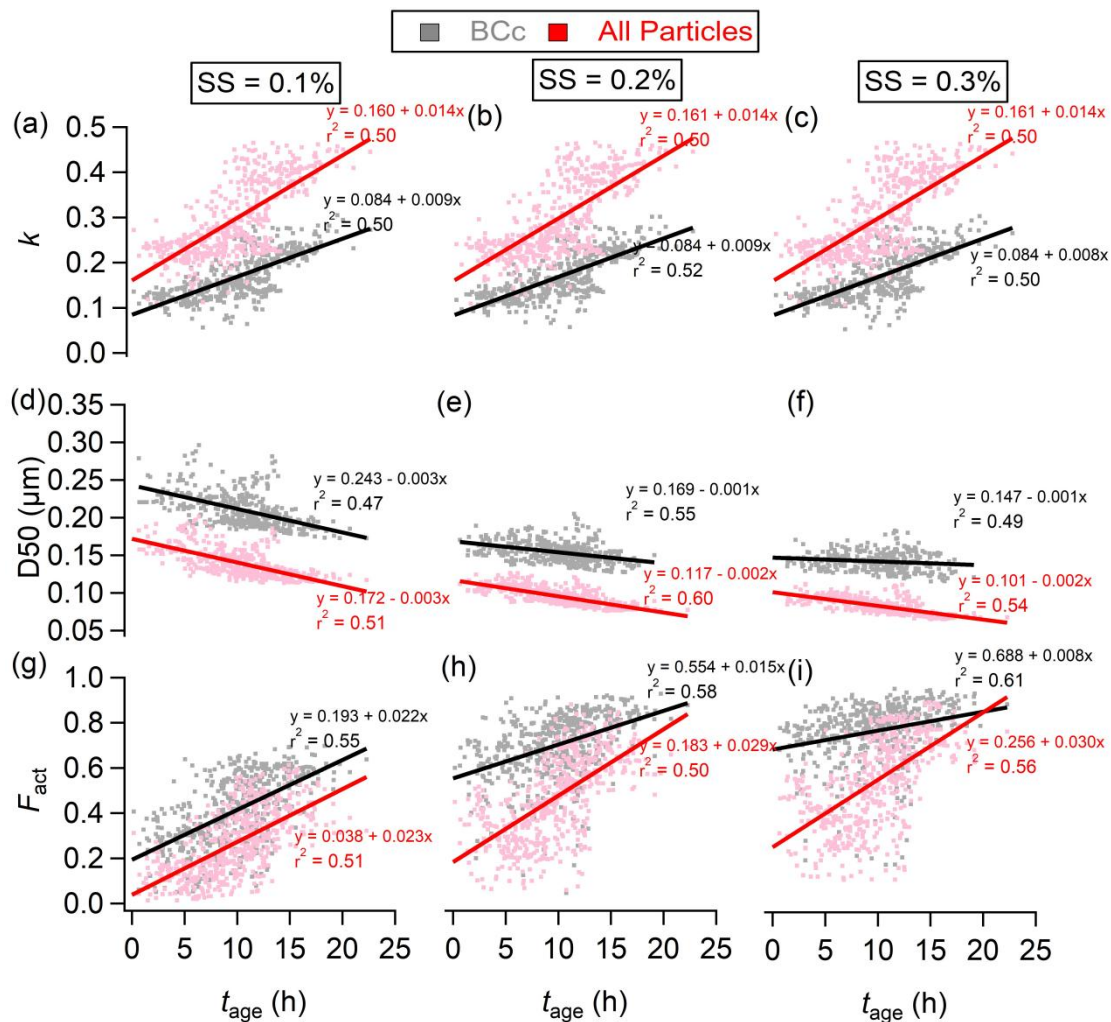
Figure 7. The evolution of hygroscopicity parameter (κ) (a-c), activation diameter (D50) (d-f), and number activation fraction (F_{act}) (g-i) with photochemical age (t_{age}) under SS at 0.1%, 0.2%, c) 0.3%. The black and red denote the BCc particles and all-particles, respectively. The lines show the least-square lineal regression.